Surface length scales and shear stress: Implications for land-atmosphere interaction over complex terrain

John D. Albertson
Department of Environmental Sciences, University of Virginia, Charlottesville

Marc B. Parlange
Department of Geography and Environmental Engineering, The Johns Hopkins University, Baltimore, Maryland

Abstract. A large eddy simulation (LES) code of the atmospheric boundary layer (ABL) has been developed and applied to study the effect of spatially variable surface properties on the areally averaged surface shear stress at the land-atmosphere interface. The LES code simulates the space and time evolution of the large-scale turbulent eddies and their transport effects in the ABL. We report here on simulations of flow over spatially variable roughness fields. The dynamics are simulated, and the resulting space-time fields are averaged to explore the effects of the surface variability length scales on the average surface shear stress, as used in large-scale models to estimate scalar fluxes, such as evaporation. We observe asymmetrical response of the smooth-to-rough and rough-to-smooth transitions, such that the effects of the transitions accumulate rather than cancel. It is shown that the presence of abrupt changes in surface roughness and the atmosphere's response to these patches create a marked dependence of the statistical structure of surface shear stress on the length scale of the surface patches. An increase in regionally averaged surface stress for decreasing horizontal patch length scale is found.

1. Introduction

Successful modeling of surface hydrologic and atmospheric processes hinges on the ability to describe the exchange of water, heat, and momentum across the land-atmosphere interface. A major concern is how to account for the effect of the spatial variability of surface conditions on scales smaller than the model grid cell. The actual total grid cell exchange is an integration of small-scale exchange processes over the area of the cell, where the physical integration is provided by the turbulent mixing in the atmospheric boundary layer (ABL). There is at present no consensus on what measures of subgrid surface properties are needed to represent the total exchange. There is hope that a better understanding of the details of this physical integration would support improved model development [*Parlange et al*., 1995, 1999; *Albertson et al*., 1996; *Dabberdt and Schlatter*, 1996].

To begin to develop a general answer to these questions demands a vast amount of information describing surface fluxes distributed in space and time over the study area and the dynamics of interaction between the surface and the atmospheric motions. Here we approach this through the application of a new three-dimensional numerical simulation code employing the large eddy simulation (LES) technique. The simulations are performed at a fine scale to examine detailed processes inside a hypothetical single larger grid cell (e.g., in a river basin or mesoscale forecasting model). The LES provides the ability to modify important characteristics (e.g., length scale of surface patches) such that we can observe their influences on the turbulence and quantify their effects on the ABL structure and areally averaged exchange rates. This is a significant departure from the conceptual modeling and Reynolds averaged modeling approaches in that the simulation code represents the space-time dynamics of the turbulent flow and transport through a time-dependent implementation of the Navier-Stokes equations on a three-dimensional (3-D) grid over the study site. Therefore the surface exchange and the turbulent mixing processes that combine to form the physical aggregation are represented by the basic equations, rather than through models. On-line averaging of the space-time fields provides measures for evaluating net regional effects to average surface fluxes.

The LES technique has proven useful for simulating boundary layer dynamics for both neutrally and unstably stratified flows [e.g., *Deardorff*, 1970a, b; *Moeng*, 1984; *Schmidt and Schumann*, 1989]. Here we focus on the surface shear stress for the neutral case in recognition of the importance of surface shearing in the removal of water vapor, heat, and volatilized contaminants from the land surface. Hence LES is employed in this study to simulate momentum exchange (i.e., surface shear stress) across a patchy surface under neutral boundary layer stratification, to examine how the flow couples the flux processes of the adjacent patches, and to identify potential implications for areally averaged exchange rates.

1.1. Surface Properties in Hydrology and Meteorology

Hydrologic and atmospheric simulations must employ grid cell level "measures" of surface properties in order to estimate the total exchange (e.g., momentum, heat, and water vapor) across the land-atmosphere interface over the surface area of each grid cell. However, the open question is what measures are most important for an accurate and parsimonious repre-

Paper number 1999WR900094.
0043-1397/99/1999WR900094$09.00

sentation of the averaged exchange processes. We explore here whether the horizontal length scale of surface variability is an important variable.

Studies of subgrid heterogeneity in the context of general circulation models (GCMs) have focused on subgrid patches at the mesoscale, with length scales of say 10–50 km [*Segal and Arritt*, 1992]. However, for physical hydrologic modeling of large catchments or regional climate analysis we are concerned with the effect of spatial variability on length scales below, say, 2 km as the grid cells may be of order 10^2–10^4 m on a side. There is a natural gap in scale between the mesoscale patches (studied as GCM subgrid processes) and the local patches (scale O 2 km) addressed here, for while the ABL adjusts fully (i.e., organizes) to each of the mesoscale patches [e.g., *Raupach*, 1991], the flux from the local patches is integrated or mixed through the ABL with coupling between patches affected by the boundary layer turbulence [*Brutsaert and Parlange*, 1992; *Parlange and Brutsaert*, 1993]. The ABL thus represents the composite effect of the local patches, including the nonlinear interaction between the patches. The surface layer flow over the patches serves to couple the flux processes over one patch to those over the adjacent patch. It is important to note that there are different mechanisms connecting these local-scale patches (i.e., turbulent transport) than those active across the mesoscale patches (i.e., mean circulation).

At present most numerical models of surface hydrologic processes and atmospheric processes account for the land-atmosphere exchange through the use of simple statistics of the surface properties. A first, and rather rough, approach to this problem has been to apply a simple linear aggregation (averaging) of the surface properties for use in estimating average grid cell exchange. These average properties are then used to estimate the average flux, an approach which ignores, by necessity, all nonlinearity and spatial coupling of the processes. A second approach, motivated by recognition of the nonlinear nature of the local exchange processes, has been to compile a frequency distribution of each surface property within each grid cell and map these through surface exchange functions in order to compute an estimate of the total grid cell exchange [e.g., *Avissar*, 1991, 1992]. However, this approach assumes that the individual surface properties (e.g., roughness, temperature, and soil moisture) are uncorrelated and assumes that the surface patches are independent of each other. In the context of the scales addressed here there is a significant body of experimental evidence to the contrary [e.g., *Brutsaert and Stricker*, 1979; *Parlange and Katul*, 1992; *Parlange et al*., 1999] since local advection provides a strong coupling between adjacent patches on the land surface for the scales of interest in hydrology.

Frustrating the efforts to model subgrid surface fluxes so far is the lack of a general understanding of the physics of land-atmosphere interaction over heterogeneous surfaces. Rather than an a priori statistical approach, attention needs to be paid to the physics and how they scale in order to identify the core set of surface measures needed to represent the flux from realistic surfaces. Here we address these questions through simulations with LES and systematic analysis of the physical processes that are interacting and combining to form the aggregate exchange. Specifically, we study whether the length scale of surface variability is a good candidate for inclusion in aggregation modeling.

In summary, the problem with the existing approaches is that they ignore the potential effect of surface length scale on exchange and the dependence between adjacent patches. For example, two surfaces with the same probability density function (pdf) of surface properties may have considerably different total surface flux over the domain because of coupling between the patches and effects of length scale of the patches on the aggregate flux.

1.2. Land-Atmosphere Processes and the Effect of Scale

The portion of the atmosphere closest to the surface reacts to a change in surface properties through the development of an internal boundary layer (IBL) just above the surface downwind of the change. In an important field experiment, *Bradley* [1968] used artificial roughness elements and measured time-averaged shear stress versus distance from a step change in roughness with drag plates. His results compared well to the theory of *Panofsky and Townsend* [1964]. While *Panofsky and Townsend*'s [1964] theory was developed with consideration of the rough-to-smooth transition, they had assumed that the reverse arrangement would have an analogous response. However, Bradley noted that the smooth-to-rough equilibrated faster than the reversed case, but he did not address possible reasons. This asymmetric response is central to our problem as it suggests that the effects of the transitions between the patches may not "average out."

Antonia and Luxton [1971] studied the structure of the IBL after a step change in surface roughness from smooth-to-rough in a wind tunnel. The IBL was found to grow at a rate controlled by the vertical diffusion of turbulent kinetic energy (TKE) from the high-production region near the surface. They found that a new equilibrium surface stress was reached at a distance well downstream of the transition. In a subsequent study of the transition downstream of a rough-to-smooth transition, *Antonia and Luxton* [1972] found strikingly different results. Over the smooth surface the transition to a new equilibrium took much longer, with the rate of growth of the IBL being markedly less than downstream of the smooth-to-rough transition. They note that this agrees generally with *Bradley*'s [1968] observations. The slow growth of the IBL over the smooth surface is attributed to influences from both the inner and outer layers. In contrast to the smooth-to-rough case, where the upward diffusion of TKE (in the internal region) controls the growth rate, the IBL growth rate following a rough-to-smooth transition is damped by the outer region's action to compensate for reduced production of TKE over the smooth wall. Hence the response for rough-to-smooth may be due to both the internal and outer regions, while the response in the reverse case may solely be due to the internal region processes. With the flow over smooth-to-rough and rough-to-smooth transitions not equilibrated in a similar manner it is reasonable to foresee that there may be net consequences from these transitions arising in the regional averaging of surface exchange.

Several other recent studies have employed Reynolds-averaged models of the surface layer to address flow over heterogeneous terrain [e.g., *Claussen*, 1991; *Klaassen*, 1992; *Kroon and de Bruin*, 1993; *Baldocchi and Rao*, 1995]. They have noted the edge effects due to the presence of the upwind field and postulated how these effects might influence the aggregate exchange over a larger area. With these Reynolds averaged approaches the mean fields are solved for with all of the turbulent motion averaged out. Therefore all variability in surface exchange is brought about by variations in the mean longitudinal velocity, which is caused by the a priori assumptions of

what happens with the transitions in surface properties. This is arguably a somewhat circular approach. Here we simulate the turbulence over heterogeneous land surfaces and observe its net effects.

There have been several LES studies of boundary layer turbulence over inhomogeneous surface conditions, such as those by *Hechtel et al*. [1990] and *Shen and Leclerc* [1995]. However, these studies focused on the resulting structure of the mixed layer turbulence, not on the areal-averaged surface exchange as in the present paper.

The rationale for the present approach is that the LES provides physically realistic 3-D representations of the ABL structure over patchy land surfaces to reveal both spatial and temporal details of the atmospheric response to surface features. This work is motivated by the need for better parameterizations of river basin scale surface fluxes and the demonstrated success of LES to simulate boundary layer dynamics [*Deardorff*, 1972; *Moeng*, 1984; *Moeng and Wyngaard*, 1984; *Krettenauer and Schumann*, 1992; *Andren et al*., 1994]. Moreover, the physical simulation and analysis of how surface patches interact with each other through the surface layer coupling holds promise for providing a physical basis for parameterizing surface heterogeneity in basin-scale land-atmosphere interaction. Here we simulate the 3-D turbulent motion and transport with variation in time and space, such that the surface stress develops a time and space distribution as a consequence of both the mean field and the turbulent field.

The specific objectives of this study are to identify spatial coupling between surface patches, identify the effect of patch scale on spatially averaged surface shear stress, and explore possible implications from the momentum case for scalar exchange. The case study described here employs modest roughness transitions to demonstrate the physics of how these local edge effects can manifest themselves in a net sense at the regional scale. Certainly more extreme roughness transitions, such as forest to agriculture, would have larger-magnitude effects; however, the processes remain the same. The stated objectives are accomplished through use of the LES code described in section 2.

2. Large Eddy Simulation

Numerical simulation of turbulence is divided into two basic classes: (1) direct numerical simulation (DNS) where all scales of the flow are resolved, from the largest energy-producing eddies down to the small energy-dissipating eddies, and (2) LES, where a range of scales is resolved, from the largest eddies down to an arbitrary cutoff size, below which the dynamics are modeled. Resolving the flow implies that the equations of motion are integrated over a discrete mesh in time and space. The term "simulation" refers here to the direct integration of the basic equations, while the term "model" is used to describe the use of closure models for the unresolved scales.

The direct numerical simulation of ABL dynamics would require the solution of the governing equations over a grid capable of resolving the dissipation scale of motion. Order of magnitude arguments suggest that this would require resolving $Re^{9/4}$ degrees of freedom, where Re is the Reynolds number [*McComb*, 1990]. As Re can be of order 10^8 in the ABL, this is equivalent to a requirement of $\sim 10^{18}$ nodes (or modes, if using spectral methods). Present computing resources limit the size of practical applications to $\sim 10^8$ degrees of freedom, thus dashing any hope of simulating all the active scales in the ABL. Consequently, the numerical efforts described here are limited to partial resolution of the turbulence through LES. A fundamental tenet of LES is that the large scales of motion are the most dependent upon the gross flow characteristics. These structures are resolved in the LES, while the eddies smaller than some scale in the inertial subrange are modeled in terms of the resolved scales. This is a natural approach; for while the inertial subrange eddies receive their energy from the larger scales, they are also rendered statistically independent of the large-scale motion and any anisotropy that it may possess through the cascading process [e.g., *Batchelor*, 1953]. Furthermore, it is the large (resolved) scales that are responsible for the transport of momentum, heat, and mass.

To account for this incomplete resolution, the equations of motion and transport must be modified. If the dissipation scales are not resolved, or otherwise accounted for, the cascading energy would accumulate in the resolved range rather than continuing down scale and ultimately being dissipated by molecular action [see, e.g., *Leonard*, 1974]. The velocity field is filtered to separate explicitly the resolved from the unresolved parts. Applying the filter to the governing equations yields equations for the resolved scales that contain certain terms involving the unresolved scales. The equations are integrated numerically with the unresolved scales parameterized by a subgrid (or subfilter) model, such as the eddy-viscosity model pioneered by *Smagorinsky* [1963]. A brief description of the LES technique in general and this code in particular is given here. For additional background on the basic equation development, see *McComb* [1990, pp. 118–124], the collection of papers by *Galperin and Orszag* [1993], and the description by *Ferzinger* [1996].

The flow variables are filtered by the explicit application of a general filter G to define the resolved field:

$$\bar{u}_i(x_1, x_2, x_3) = \oint U_i(x_1', x_2', x_3') \cdot G(x_1 - x_1', x_2 - x_2', x_3 - x_3')\, dx_1' dx_2' dx_3' \quad (1)$$

such that the total instantaneous value may be represented as the sum of filtered and subgrid components:

$$U_i = \bar{u}_i + u_i' \quad (2)$$

where $\bar{u}_i$ is the resolved portion of the x_i direction velocity component and u_i' is the subgrid or unresolved portion. Both $\bar{u}_i$ and u_i' vary in time and space. For this effort we restrict consideration to homogeneous filters, i.e., $G(x_1 - x_1', x_2 - x_2', x_3 - x_3') = G(\Delta x_1, \Delta x_2, \Delta x_3)$, such that the filtering process commutes with differentiation [*Aldama*, 1990]. The equations are nondimensionalized by a global boundary layer length scale z_s (e.g., depth of ABL or height of capping inversion) and the friction velocity u_*.

The final, dimensionless, filtered equations governing transport of momentum in a neutrally stratified boundary layer under the Boussinseq assumption are

$$\partial_i \bar{u}_i = 0 \quad (3)$$

$$\partial_o \bar{u}_i + \overline{\bar{u}_j(\partial_j \bar{u}_i - \partial_i \bar{u}_j)} = -\partial_i \bar{p} + F_p \delta_{i1} - \partial_j \tau_{ij} \quad (4)$$

with the subgrid stress (requiring closure) represented by

$$\tau_{ij} = R_{ij} - \tfrac{1}{3} R_{kk} \delta_{ij} \qquad R_{ij} = \overline{\bar{u}_i u_j'} + \overline{u_i' \bar{u}_j} + \overline{u_i' u_j'} \quad (5)$$

$$\bar{p} = \frac{\overline{p^1}}{\rho_o} + \frac{1}{3}R_{kk} + \frac{1}{2}\overline{\bar{u}_j\bar{u}_j} \tag{6}$$

Equation (6) is a modified pressure variable that contains (1) the Boussinesq kinematic pressure, (2) the trace of the subgrid stress tensor to account for the difference between R_{ij} and τ_{ij}, and the TKE to balance the extra term on the left-hand side of (4), which is written in rotational form to conserve kinetic energy as well as mass [*Orszag and Pao*, 1974; *Ferzinger and Perić*, 1996, p. 156]. The subgrid stress is closed with an eddy-viscosity model

$$\tau_{ij} = -2\nu_T\bar{S}_{ij} \tag{7}$$

with *Smagorinsky*'s [1963] formulation for the eddy viscosity

$$\nu_T = C_1 q l = (C_s l)^2\sqrt{2\bar{S}_{ij}\bar{S}_{ij}} \tag{8}$$

where $\bar{S}_{ij}$ is the resolved strain rate tensor given by

$$\bar{S}_{ij} = \frac{1}{2}(\partial_j\bar{u}_i + \partial_i\bar{u}_j) \tag{9}$$

Note that δ_{ij} (1 for $i = j$ and 0 for $i \neq j$) is the Kronecker delta, ∂_o is the partial derivative operator with respect to time, ∂_i is the partial derivative operator with respect to the x_i direction (i.e., $\partial/\partial x_i$), $\overline{p^1}$ is the filtered version of the original static pressure, ρ_o is the reference density used in the Boussinesq assumption, F_p is the mean streamwise pressure gradient (constant forcing), the coordinate system is Cartesian ($x_1 = x$, $x_2 = y$, and $x_3 = z$), with z being normal to the wall and x being along the mean wind direction, C_s is the Smagorinsky constant (taken as 0.2 in this study), l is the mixing length representative of the scale at which energy cascades from the resolved to the unresolved scales, and summation is implied on all repeated subscripts (i.e., $\partial_j\partial_j\bar{u}_i = \partial_1\partial_1\bar{u}_i + \partial_2\partial_2\bar{u}_i + \partial_3\partial_3\bar{u}_i$). Note that Coriolis effects have been neglected as our focus is on surface layer turbulence, which is generally insensitive to the Earth's rotation [e.g., *Kaimal and Finnigan*, 1994].

Therefore we have three momentum equations for the three velocity components, a continuity equation for the pressure, and nine subgrid momentum flux closure equations for the nine subgrid momentum fluxes. The pressure field in the momentum equation is not a thermodynamic variable but rather a dynamic variable that serves to maintain a divergence free, or incompressible, velocity field. Consequently, we deduce a pressure field to force the velocity divergence to vanish by taking the divergence of the momentum equation and applying the continuity equation. This leaves us with a Poisson equation for pressure. Hence the system is closed pending prescription of boundary and initial conditions.

2.1. Numerics

The horizontal directions are treated with pseudospectral differentiation, and the vertical direction is treated with finite differences. The pseudospectral numerics are after *Orszag* [1971a, b], and the mixed approach with finite differences in the wall-normal direction is after *Moin et al*. [1978].

A discrete function may be represented by either its values in physical space or its Fourier counterpart through the expansion in terms of trigonometric functions

$$\bar{u}_i(x, y, z) = \sum_{k_x}\sum_{k_y}\hat{u}_i(k_x, k_y, z)e^{i(k_x x + k_y y)} \tag{10}$$

where $\hat{u}_i$ is the complex Fourier amplitude associated with the physical space variable $\bar{u}_i$, k_x and k_y are the wavenumbers in the x and y directions with summations ranging over the integer wavenumbers $-N_x/2 + 1 \leq k_x \leq N_x/2$ and $-N_y/2 + 1 \leq k_y \leq N_y/2$ (where N_x and N_y are the numbers of nodes in each the x and y direction), and $i = \sqrt{-1}$. For this 2-D discrete transform it is understood that x and y assume values only at the quadrature points: $x = 2\pi(i - 1)/N_x$; $y = 2\pi(j - 1)/N_y$; and z remains unconstrained. The transform in (10) is invertible (i.e., $\bar{u}_i \Leftrightarrow \hat{u}_i$) since it is linear and complete in the sense of a Hilbert space [*Canuto et al*., 1988]. Recall that $\bar{u}_i$ is a filtered field such that it is fully resolved by the number of modes employed in this finite or truncated expansion (10).

Taking the x and y partial derivatives of each side of (10) yields

$$\frac{\partial\bar{u}_i(x, y, z)}{\partial x} = \sum_{k_x}{}' \sum_{k_y}{}' [\hat{u}_i(k_x, k_y, z)(ik_x)]e^{i(k_x x + k_y y)} \tag{11}$$

$$\frac{\partial\bar{u}_i(x, y, z)}{\partial y} = \sum_{k_x}{}' \sum_{k_y}{}' [\hat{u}_i(k_x, k_y, z)(ik_y)]e^{i(k_x x + k_y y)} \tag{12}$$

where $\Sigma'_{k_x i}$ is to denote a sum over all wavenumbers except the Nyquist values (i.e., $k_x = N_x/2$ or $k_y = N_y/2$). For convenience we can represent the terms in the square brackets as $\hat{u}_i'^x$ for (11) and $\hat{u}_i'^y$ for (12); these primed amplitudes are in fact the Fourier counterparts to the physical space derivatives, i.e., $\partial\bar{u}_i(x, y, z)/\partial x \Leftrightarrow \hat{u}_i'^x$ and $\partial\bar{u}_i(x, y, z)/\partial y \Leftrightarrow \hat{u}_i'^y$. The process for computing the derivatives in physical space is by taking a known set of $\bar{u}_i(x, y, z)$, computing the set $\hat{u}_i(k_x, k_y, z)$ from the equality in (10), modifying $\hat{u}_i$ to form $\hat{u}_i'^x$ and $\hat{u}_i'^y$, and finally, computing the set of $\partial\bar{u}_i(x, y, z)/\partial x$ and $\partial\bar{u}_i(x, y, z)/\partial y$ from (11) and (12). This approach is applied to horizontal planes of nodes (i.e., constant z) taken from the 3-D mesh of nodes in the flow domain. Second derivatives are also available from application of the partial derivative operators to (11) and (12), yielding amplitudes $\hat{u}_i''^x$ [$= \hat{u}_i(k_x, k_y, z)(-k_x^2)$] and $\hat{u}_i''^y = [\hat{u}_i(k_x, k_y, z)(-k_y^2)]$ for the second derivatives. The derivatives with respect to the vertical direction are by second-order accurate, centered finite differencing on a vertically staggered grid that references the vertical velocity component to midnodes, located between the main nodes that contain the remaining primitive variables.

The Poisson equation for pressure is solved numerically using the spectral transform in the horizontal and finite differences in the vertical with a tridiagonal solver. The time advancement is by a fully explicit second-order Adams-Bashforth scheme

$$\frac{u_i^{t+\Delta t} - u_i^t}{\Delta t} = \frac{3}{2}\overline{\mathrm{RHS}_i}^t - \frac{1}{2}\overline{\mathrm{RHS}_i}^{t-\Delta t} \tag{13}$$

where RHS_i is written for the discrete (numerical) form of $-\overline{\bar{u}_j(\partial_j\bar{u}_i - \partial_i\bar{u}_j)} - \partial_i\bar{p} + F_p\delta_{i1} - \partial_j\tau_{ij}$ and superscripts are used for time level referencing. This approach has been shown to be both accurate [*Gao and Leslie*, 1990] and efficient, with a computational mode that tends to damp favorably [*Haltiner and Williams*, 1980, p. 151].

2.2. Boundary Conditions

The horizontal directions are assigned periodic boundary conditions such that for any primitive flow variable A we have

$$A(x + mL_x, y + nL_y, z) = A(x, y, z) \quad (14)$$

where L_x and L_y are the domain dimensions in the x and y directions and m and n are signed integers. These longitudinal and lateral boundary conditions are implemented implicitly with the Fourier numerics. The top boundary is positioned well above the top of the boundary layer and assigned a condition of vanishing vertical gradients (no stress) and no flow through the boundary such that at top,

$$\partial_3 \bar{u}_i = \bar{u}_3 = 0 \quad (15)$$

The bottom boundary is far more critical to the structure of the turbulence than the sides and top as the mechanical turbulence is produced as a result of drag at the wall. The surface shear stress is computed over the bottom boundary as a function of the prescribed local roughness length z_o and near-surface resolved velocity by integrating the logarithmic velocity gradient from $z = z_o$ to the height of the first node above the wall to obtain

$$\tau_w = -\left[\frac{U_r k}{\ln (z/z_o)}\right]^2 \quad (16)$$

where U_r is the local resultant resolved velocity $[(\bar{u}_1^2 + \bar{u}_2^2)^{1/2}]$ at height z. Following *Schmidt and Schumann* [1989], we partition the stress among its x and y components as

$$\tau_{i,3}|_{\text{wall}} = \tau_w\left[\frac{\bar{u}_i(z)}{\bar{U}_r(z)}\right] \qquad i = 1, 2 \quad (17)$$

While it is understood that this type of wall function has its roots as a relationship between mean values, it is often extended to instantaneous values in boundary layer simulations [e.g., *Moeng*, 1984; *Mason and Callen*, 1986; *Schmidt and Schumann*, 1989]. It is used here as a wall-specific subgrid model that relates instantaneous resolved velocity fields to local instantaneous shear stress. Because the mesh is staggered, with vertical velocity values assigned to nodes located vertically offset from the longitudinal and transverse velocity nodes, we need not employ no-slip boundary conditions for $\bar{u}_1$ and $\bar{u}_2$. The vertical velocity boundary condition is simply

$$\bar{u}_3 = 0 \qquad z = 0 \quad (18)$$

The pressure field receives periodic horizontal boundary conditions and vertical boundary conditions from considerations of the vertical momentum equation written at the wall and the top of the domain. This code has been successfully validated [*Albertson*, 1996] against the results presented by *Andren et al.* [1994], who compared four established LES codes for simulation of the neutral ABL.

3. A Suite of Simulations

In support of the objectives described above, three ABL simulations were performed over patchy surfaces of varying patch length. By varying the length scale of the patches we investigate how the scale of the surface heterogeneity affects the domain-aggregated surface exchange of momentum.

3.1. General Flow Description

While the patch scale varies between the three simulations, all other gross flow characteristics remain unchanged. The depth of the simulation domain is 700 m, which is reasonable for a case such as that studied here without surface heating. The scaling height was chosen as $z_s = 500$ m, such that the horizontal dimensions of the domain are 3140 m (i.e., $2\pi z_s$) in the x and y directions. The domain is spanned by 64 nodes in the x direction, 32 nodes in the y direction, and 100 nodes in the z direction. Hence the nominal dimensional mesh spacing is 50 m in the x direction, 100 m in the y direction, and 7 m in the z direction. Note that because of the staggered mesh, the first plane of nodes above the wall for $\bar{u}_1$ and $\bar{u}_2$ is at $\Delta z/2$ (= 3.5 m).

The initial conditions are a modified logarithmic velocity profile with a prescribed TKE profile superimposed on the mean profile. The mean profile is logarithmic in the surface layer but is forced to reach a zero vertical gradient at z_s and remain at a constant velocity above this height. The dimensionless momentum roughness ($z_o = 0.1$ m/z_s) was selected to correspond to an effective roughness [*Claussen*, 1991] representative of the overall effect of the prescribed patchy surface, which is described below. The initial transverse and vertical velocities have zero mean values at all heights. The initial vertical profile of resolved TKE is again taken from the LES comparison paper of *Andren et al.* [1994, Table A.1]. The instantaneous initial velocities $\bar{u}_i(x, y, z)$ are obtained by distributing the TKE randomly between the components and in space onto the mean profiles. The sole purpose of this initial TKE profile is as a disturbance field to begin the production of turbulent eddies and their cascade to smaller and smaller eddies.

A dimensionless time step of 0.0005 was used, which corresponds to a dimensional time step of roughly 0.5 s. The spinup period was chosen to be 10,000 time steps for each simulation, corresponding to 5 dimensionless time units or a physical period of roughly 1.4 hours. All memory of the initial disturbance profile is lost through this spin-up period, and the turbulence moments are dependent on the boundary conditions and the governing Navier-Stokes equations. The statistics for the comparison below were computed over a simulation period of 3000 time steps (e.g., 0.5 hours of physical turbulence), immediately following the spin-up period. For each of the simulations the spin-up was satisfactorily long to reach stationary statistics during the 3000 step analysis period.

3.2. Varying Surface Properties

The simulations are of turbulent ABL flow over surfaces of patchy roughness, representative of alternating patches of medium height (1–2 m) vegetation (rough) and grass (smooth). In all cases the patches alternate between smooth and rough, starting with a smooth patch at $x = 0$. The roughness fields are homogeneous in the y direction (i.e., lateral stripes of constant roughness). The dimensional momentum roughness length is 0.025 m for the smooth patches and 0.25 m for the rough patches; the transitions between the patches are perfectly abrupt. The surface roughness affects the flow through the boundary flux equation. We reiterate that this is a moderate roughness transition used strictly to demonstrate a physical process and its potential for regional scale effects.

3.3. Case Comparison

The sole difference between the three simulations is that case I has two surface patches (i.e., 1 smooth and 1 rough), case II has four patches, and case III has eight patches. The length scales of the individual patches are 1570 m for case I, 785 m for case II, and 390 m for case III. In the following section we first explore some basic results from the simulations and then examine the effects of the patchy surface roughness

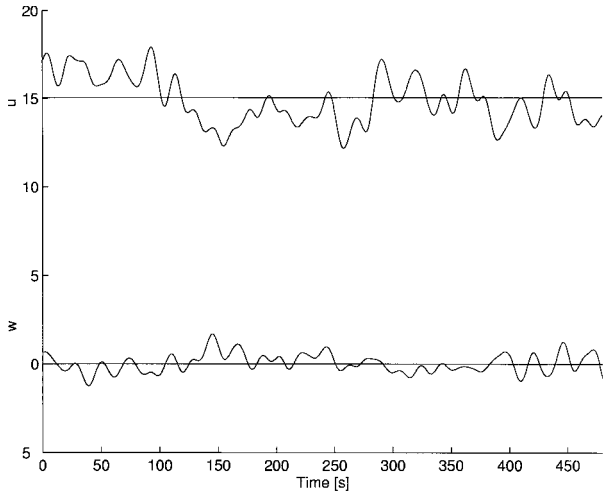

Figure 1a. (top) A time series of the streamwise velocity component at a single node in the flow domain and (bottom) a time series of the vertical velocity component at the same node.

on the structure of the flow and on the areally averaged exchange rates.

4. Results and Discussion

We are concerned with the surface stress due to the downward flux of momentum to the land surface from the ABL flow. In the boundary layer this downward flux manifests itself as a negative correlation between the longitudinal and vertical velocity fields (i.e., $\overline{u_1 u_3} < 0$). We see this relationship in Figure 1a by examining a time series of the longitudinal ($U/u_* = \bar{u}_1$) and vertical ($W/u_* = \bar{u}_3$) velocity components at a single location (x, y, z) in the flow. The negative correlation between these two time series is evidence of the downward flux of momentum through this point. For example, notice that in the first 100 s of the time series at this location there is a faster than average longitudinal velocity while the fluid is generally moving downward. This case where $U' > 0$ and $W < 0$ is referred to as a "sweep," where the high-velocity fluid is carrying momentum down toward the wall. In the second 100 s there is a slower than average longitudinal velocity while the fluid moves upward. This is an "ejection" ($U' < 0$ and $W > 0$) of low-momentum fluid into the higher regions of the boundary layer. The net effect of these two events is a downward flux of momentum. Figure 1a is also instructive in that it depicts the large-scale nature of the resolved velocity, with the smallest timescales of the motion being several tens of seconds.

This correlation between the $\bar{u}_1$ and $\bar{u}_3$ fields is depicted further in the joint pdf of these two variables on the basis of observations of $\bar{u}_1$ and $\bar{u}_3$ through the full simulation time and the full horizontal extent at $z = 5\Delta z$ in Figure 1b. The correlation between these two fields is marked by the elliptical nature of the pdf, and the downward direction of the momentum flux is marked by the negative slope of the major axis of the ellipse. The events captured in the upper left quadrant are ejections, and the events in the lower right quadrant are sweeps.

Figure 2 shows the power spectrum of the longitudinal velocity depicting how the resolved longitudinal velocity fluctuations scale with respect to eddy size in the wave (or frequency) domain. The numerical values on the k axis represent the number of full waves of size k^{-1} that would fit inside the longitudinal extent of the domain. The majority of the velocity variance is, in fact, held by the large-scale motion (low wavenumbers) that is scaling with the k^{-1} slope as described by *Katul et al*. [1995], and the smaller resolved scales ($k > 10$) do appear to be approaching the power law scaling $k^{-5/3}$ representative of *Kolmogorov*'s [1941] inertial subrange. Thus the simulated turbulence meets two important and necessary, but not sufficient conditions for a fully developed turbulent flow [see *Tennekes and Lumley*, 1972].

An instantaneous vertical cross section of the $\bar{u}_1$ field is shown in Plate 1 to provide a spatial image of the sweep and ejection process whereby momentum is transported (in a net sense) toward the land surface. Note the excursions of low-

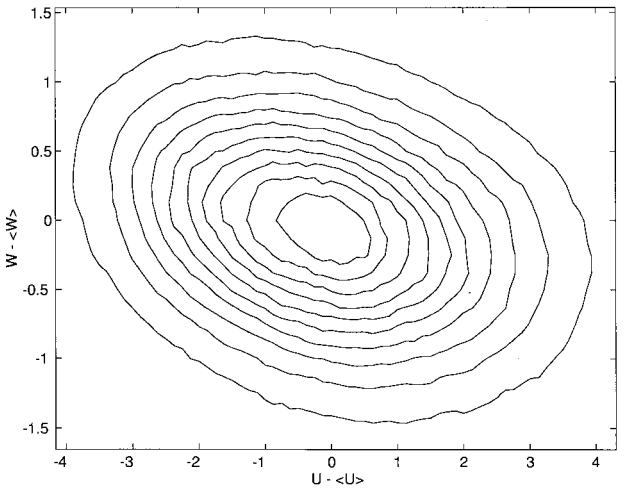

Figure 1b. A joint probability density function (pdf) of the departures of the streamwise and vertical velocity components from their time averages, where $\langle\ \rangle$ is employed to denote a time average.

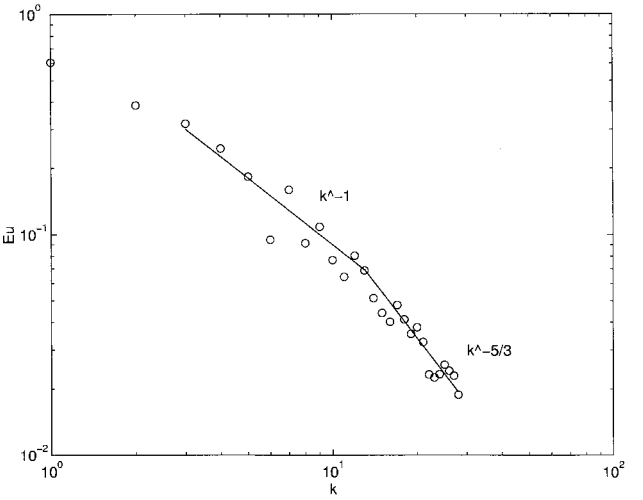

Figure 2. The power spectral density of the streamwise velocity fluctuations (Eu) in the surface layer. The circles mark the observed spectral density. The solid line marks the predicted scaling. Here k is a dimensionless wavenumber, with low values of k implying larger eddies and high values implying smaller eddies.

Plate 1. An instantaneous x-z cross section of the streamwise velocity field. The dark regions are low-momentum fluid and the bright regions are high-momentum fluid.

momentum fluid (dark) into the outer regions and the sweeps of higher-momentum fluid (light) into the near-wall region. The surface stress is the ultimate representation of this momentum flux across the surface.

The instantaneous resolved stress (or momentum flux) and the instantaneous subgrid stress are combined and averaged in time and over the y direction to provide a time-averaged picture of how the total downward momentum flux is affected by the presence of the patchy surface roughness. Plate 2 shows the structure of the normalized stress (or downward momentum flux divided by squared friction velocity) over the x and z directions for the four surface patches of case II. The first and third patches from the left edge of Plate 2 are smooth, and the second and fourth are rough. The flux over the leading edge of each patch is affected through the dynamics of the flow by the presence of the upwind patch. The near-surface fluid is moving faster on average over the smooth patches than over the rough patches, so as it moves from smooth to rough, there is an

Plate 2. An orthogonal projection of an x-z cross section of Reynolds stress. The smooth patches are noted by the low-stress surface regions, and the rough patches are below the high-stress regions. The blending out of these patches through the flow is shown clearly here, with the steady divergence of the stress with height being rather homogeneous above the so-called blending layer.

increased stress over the leading edge, which is steadily diminished as the fluid slows to the rough-patch equilibrium. Over the leading edge of the smooth patch the fluid is moving slowly from the effect of the upwind rough surface, causing the reduced stress, which is steadily increased as its smooth-surface equilibrium value is approached.

Having established the general behavior of the simulated flow, we now examine and compare the three cases in the context of the stated objectives. The streamwise structure of the longitudinal velocity $\bar{u}_1$ averaged over y and t at the first node level above the wall ($z = \Delta z/2$) is shown for the three cases in Figure 3. There are two important features to note in Figure 3: (1) how the transition region, in which the velocity is significantly different from its equilibrium patch value, represents a relatively larger portion of the total patch size for the small patches and (2) how the rough patch equilibrates over a shorter distance than does the smooth patch.

We study this second point in more detail with Figure 4, where from the case I results we plot the difference between the time-averaged streamwise velocity and its equilibrium value for the smooth and rough patches versus distance from the leading edge of the patch. The circles were obtained by subtracting from the rough patch series of Figure 3 the value that the streamwise velocity asymptotes to over the rough patch; hence in this form it asymptotes to zero; the xs were obtained similarly but for the smooth patch; the solid line is the difference between the two derived series. Case I is used here to show the structure of these series over extended fetch from the transition. Note from comparing the cases in Figure 3 that cases II and III are well represented by the left side of Figure 4 since (with respect to near-surface averaged wind velocity) these two cases are mainly foreshortened versions of the longer case. This asymmetric trend toward equilibrium was noted in the wind tunnel experiments of *Antonia and Luxton* [1971, 1972]. One important qualification needs to be made here: Antonia and Luxton's smooth wall is truly "smooth" in the fluid mechanics sense of the term, whereas we are studying what is technically a rough-to-rough transition where the magnitude of the roughness changes at the interface. Nonetheless, their observations are qualitatively similar to the present ones derived from LES, and their explanations for the asymmetry of

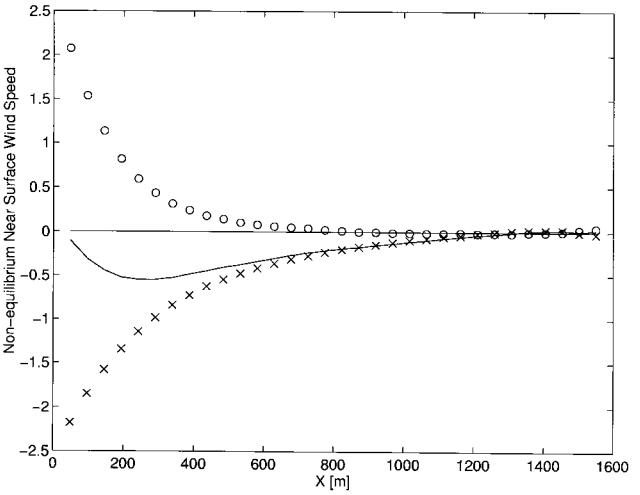

Figure 4. Nonequilibrium near-surface wind speed versus fetch. The circles (crosses) show the departure of the average streamwise velocity from its equilibrium value over the rough (smooth) patch versus distance from the leading edge of the patch. The solid line is the difference between the smooth patch values (crosses) and the rough patch values (circles).

response seems equally relevant to the present case. It is encouraging to note that the LES, through simulating the interaction of the turbulent boundary layer and the wall, is capable of capturing this effect. Note from the solid line that the departure from equilibrium is nearly everywhere greater over the smooth patch than over the rough patch. With the LES results it is possible to tie this result to the structure of the surface stress over the patches and to the relationship between the areally averaged surface stress and the length scale of the surface variability. We discuss this below.

Figure 5 shows the corresponding longitudinal structure of the surface stress for the three cases (averaged over y and t). Note that the positive nonequilibrium velocity increment ΔU over the leading edge of the rough patch translates into a much larger stress increment than does the slightly larger magnitude but oppositely signed velocity increment over the smooth sur-

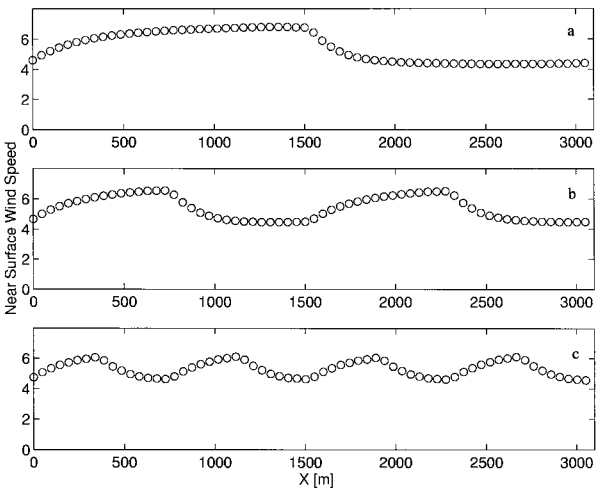

Figure 3. The average streamwise velocity at the plane of nodes closest to the wall (averaged over y and t): (a) the two-patch, (b) the four-patch, and (c) the eight-patch cases.

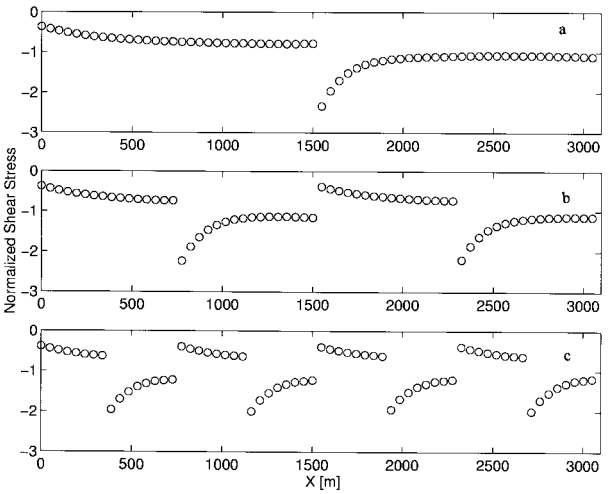

Figure 5. The average surface shear stress averaged over y and t: (a) the two-patch, (b) the four-patch, and (c) the eight-patch cases.

face. This is due to the relationship between the squared near-surface velocity and the surface stress. Note that with LES we have the average surface stress arising from a time and space distribution of surface stress that is derived from the time and space distribution of the near-surface velocity; that is, it is not computed as a simple relationship between mean quantities as with the Reynolds averaged models. This can be quite important in light of the quadratic relationship. As with the mean near-surface velocity, the smaller patch cases appear as foreshortened versions of the long patch case. From Figure 5 it is apparent that the shorter patch cases have a larger fraction of their surface area in the transition region than the long patch case, which has an essentially constant stress over the majority of each patch.

As a minor point, but encouraging with respect to the accuracy of the simulation, we observe that the slight decrease in stress just upstream of the smooth-to-rough transition and the slight increase in stress just upstream of the rough-to-smooth transition are in qualitative agreement with the detailed analysis of the transition region performed with the stream function vorticity model by *Claussen* [1987]. On the smooth-to-rough transition this can be explained by the slower flow region over the rough surface acting as a barrier to the incoming flow. Just prior to the rough-to-smooth transition the fluid is beginning to speed up to maintain continuity with the faster flow over the smooth patch. Although Claussen's study focused on the region upstream of the step change, it did note that a new equilibrium stress was not yet reached by the end of the study region, a distance of $600z_o$ downstream from the transition (equivalent to O 150 m over our rough surface).

In Figure 6 we compare the departures from patch equilibrium values for the stress over the rough and smooth patches in case I (as with the velocities in Figure 4). Here we see a combination of effects: the slower trend toward equilibrium over the smooth patch is evident along with the accentuated

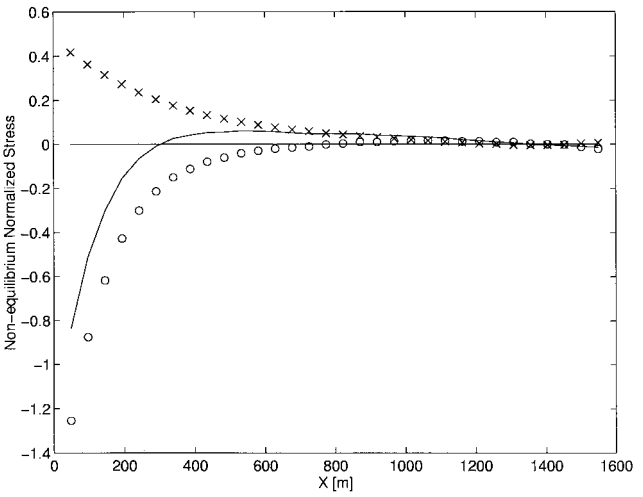

Figure 6. Nonequilibrium surface shear stress versus fetch. The circles (crosses) show the departure of the average surface stress from its equilibrium value over the rough (smooth) patch versus distance from the leading edge of the patch. The solid line is the difference between the smooth patch values (crosses) and the rough patch values (circles). Note that as the surface shear stress is expressed as a negative quantity, the negative values reflect regions where the stress is greater than its equilibrium value.

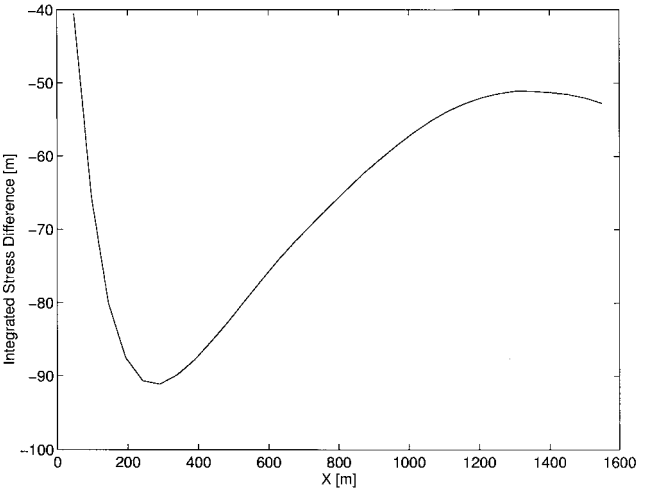

Figure 7. The integration of the solid line from Figure 8 with respect to x. This depicts the total stress increment due to the presence of smooth and rough patches as a function of patch size.

effects on the stress at the leading edge from the positive velocity increments (and quadratic stress relationship) over the rough patch. This gives rise to a difference in the nonequilibrium stress series between the rough and smooth series (solid line) that crosses the origin (unlike the velocity difference that was everywhere in favor of the smooth patch). The leading edge has a larger nonequilibrium stress increment over the rough patch; an equality is reached somewhat downstream of the leading edge, and finally, the departure over the smooth surface is greater over the interior region of the patch. In effect, there is a partial canceling of effects when integrated over the full large patch.

This is explored with a running integration of the difference between the nonequilibrium stress with respect to x in Figure 7. For any value of x on Figure 7 the ordinate marks the area under the solid line in Figure 6 to the left of x. Note that the maximum integrated nonequilibrium stress difference is found for a patch length of 200–300 m, and the total effect is realized by x $\approx$ 1000 m such that the net stress difference from equilibrium does not increase for patch lengths $>$1 km. These results are intended to demonstrate the general effects of the patchy surface on the areally averaged exchange; quantitative interpretation of the fetch distances should be considered in terms of a distance variable normalized by z_o. They are not presented in that manner here because of difficulty in intercomparing between the smooth and rough patches. For the present concern of shear stress we note that *Taylor*'s [1970] modeling results suggested a transition following a change in surface roughness extending several orders of magnitude greater than z_o, which is a similar order of magnitude as seen here.

Figure 8 shows the pdf of the surface stress sampled over x, y, and t for each of the three cases. The distributions widen as the patch size is decreased from case I to case III. This is explained by the increasing fraction of the domain affected by transition areas for the smaller patch sizes. Hence there is a noticeable relationship between the length scale of surface roughness variability and the statistical structure of the instantaneous surface stress.

At its most simple form this relationship results in depen-

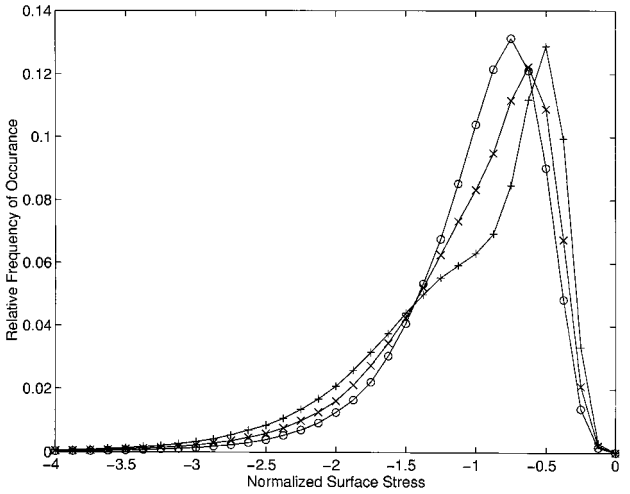

Figure 8. The pdf of surface shear stress for the two-patch case (pluses), the four-patch case (crosses), and the eight-patch case (circles).

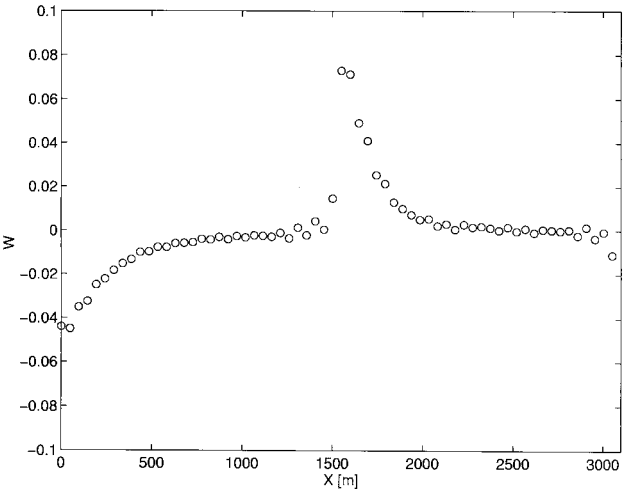

Figure 10. The average vertical velocity at the plane of nodes closest to the wall (averaged over y and t) for the two-patch case.

dence of the average surface stress on the length scale of the surface patch, as shown in Figure 9. The decrease in patch size is increasing the magnitude of domain-averaged surface stress because of the interaction of adjacent patches through the coupling affected by the surface layer turbulence and the asymmetric response noted above. Thus we see that as hypothesized earlier, surfaces with identical pdfs of surface properties but differing surface length scales are likely to have different areally averaged exchange rates. Note that the surfaces studied here have only moderate roughness differences between the rough and smooth regions. Certainly, greater effects can be expected for more drastic differences in practice.

The presence of patches of surface roughness is also noticed in the mean vertical component of the velocity. In Figure 10 the air is shown to be moving upward on average over the leading edge of a rough patch and to be moving downward on average over the leading edge of a smooth patch. This is due to the conservation of mass and the (1-D) nature of the surface variability (i.e., homogeneous in y). The mean wind is slowing over the rough patch, i.e., $\partial_1 \bar{u} < 0$, which, through the conservation of mass ($\partial_i \overline{u_i} = 0$), is creating an increase in the vertical wind velocity with height, $\partial_3 \bar{w} > 0$. The converse is occurring over the smooth patch. Figure 10 is included to highlight the implications for scalar flux near the leading edge of surface patches. Following the transition to a rough patch, there may be enhanced upward scalar flux because of a combination of increased surface shearing and the mean upward motion in this transition region. Also, in the leading edge region of a smooth surface there is a reduced shear stress and a net downward motion serving to dampen the vertical turbulent flux.

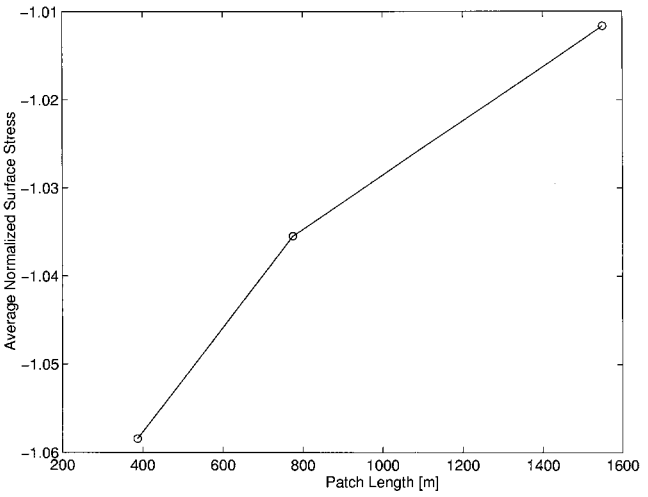

Figure 9. Domain-averaged surface shear stress versus patch scale.

5. Conclusions

Motivated by the need for an improved understanding of the relationship between the spatial structure of surface properties and the net exchange across the land-atmosphere interface, we used a LES code to study the vertical momentum flux in a neutrally stratified turbulent boundary layer over patchy surfaces. The scales of interest were limited to those within a single grid cell of a typical regional-scale simulation model (i.e., O 2 km). The coupling of surface patches in this range of scales is due to the dynamics of the inner region of the atmospheric boundary layer. The simulated boundary layer turbulence was shown to capture the space and time structure of this flow-induced coupling of adjacent surface patches, including the presence of important features noted in previous investigations of wind tunnel and ABL experiments [e.g., *Bradley*, 1968; *Antonia and Luxton*, 1971, 1972]. Through the simulations we were able to explore the net effects to regional-scale fluxes from the asymmetrical response of the surface patch transitions.

Most importantly, through a combination of (1) the different rates at which smooth and rough surfaces reach equilibrium velocities and (2) the increased effect of positive velocity departures on surface stress vis-a-vis negative departures, the simple presence of roughness transitions was shown to increase the average surface shear stress. The presence of edges and the corresponding transition regions inside each patch were shown to create a marked dependence of the statistical structure of surface stress on the length scale of the surface patches. At its

simplest level this structure manifests itself in a clear increase of average surface stress with decreased length scale of surface patches over the range of patch scales studied (even for the moderate z_o differences). Therefore we are able to conclude that the pdf of surface properties over a model grid cell is an incomplete representation of the surface properties for an accurate accounting of the average surface exchange over the cell. Future models of land-atmosphere interaction may offer improved performance by also accounting for the length scale over which the surface properties vary.

It was demonstrated that the maximum stress increment due to the presence of the edge is found for a relatively small patch length (200–300 m for the roughness used here) and that the increment added per edge is constant for patch lengths greater than some value of the order of a kilometer. The slowing of the mean wind over the rough surface was shown through the conservation of mass, to induce a mean upward motion. This mean upward motion and the increased surface stress over the leading edge of a rough patch will combine to increase further vertical scalar flux over this region. For the case of evaporation over an irrigated cropped surface downwind of a bare arid region this mechanical effect may be in addition to otherwise increased evaporation rates from local advection of hot, dry air over the cool, wet surface.

The implications of the processes demonstrated in this work are mainly relevant to modeling studies seeking to parameterize the spatial average surface fluxes over large grid cells. These edge effects would be implicitly included along with other near-surface flow effects in regional-scale flux observations made well up in the boundary layer. For either type of application, modeling or observations, we note that the increase in stress found for this moderate roughness transition is roughly equivalent to that realized from a 15% change in an effective roughness value (as defined by an error analysis that differentiates the log law with respect to z_o).

Although quantitative values presented in the final figures may be limited to the particular example of roughness lengths considered, the general structure of the results and the basic relationships between the patch scales and the surface stress statistics should hold true in a general sense. In fact, we anticipate that the magnitude of the effect would be considerably larger for the types of roughness transitions often encountered in practice (e.g., agricultural fields and forests). The effects demonstrated in this study are supported by the corroborative evidence found in the experimental literature, reviewed above for the response of velocity and surface stress fields to roughness transitions. With this fundamental relationship established, future studies are planned to explore the effects of boundary layer depth and density stratification on this relationship.

Acknowledgments. This work was funded by the NASA Earth System Science Fellowship Program and the NSF under EAR 9304331. Additional assistance was provided by a faculty startup grant from the University of Virginia. We are thankful for the assistance of W. Kollmann, R. Shaw, and several anonymous reviewers.

References

Albertson, J. D., *Large Eddy Simulation of Land-Atmosphere Interaction*, Ph.D. thesis, 185 pp., Univ. of Calif., Davis, 1996.

Albertson, J. D., G. Kiely, and M. B. Parlange, Surface fluxes of momentum, heat, and water vapor, in *Global Environmental Change*, vol. 45, *Radiation and Water in the Climate System*, *NATO ASI* Ser. 1, edited by E. Raschke, pp. 59–82, Springer-Verlag, New York, 1996.

Aldama, A. A., *Filtering Techniques for Turbulent Flow Simulation*, *Lecture Notes Eng*. vol. 56, edited by C. A. Brebbia and S. A. Orszag, 397 pp., Springer-Verlag, New York, 1990.

Andren, A., A. R. Brown, J. Graf, P. J. Mason, C.-H. Moeng, F. T. M. Nieuwstadt, and U. Schumann, Large-eddy simulation of a neutrally stratified boundary layer: A comparison of four computer codes, *Q. J. R. Meteorol. Soc*., *120*, 1457–1484, 1994.

Antonia, R. A., and R. E. Luxton, The response of a turbulent boundary layer to a step change in surface roughness, 1, Smooth to rough, *J. Fluid Mech*., *48*, 721–761, 1971.

Antonia, R. A., and R. E. Luxton, The response of a turbulent boundary layer to a step change in surface roughness, 2, Rough to smooth, *J. Fluid Mech*., *53*, 737–757, 1972.

Avissar, R., A statistical-dynamical approach to parameterize subgrid-scale land-surface heterogeneity in climate models, *Surv. Geophys*., *12*, 155–178, 1991.

Avissar, R., Conceptual aspects of a statistical-dynamical approach to represent landscape subgrid-scale heterogeneities in atmospheric models, *J. Geophys. Res*., *97*, 2729–2742, 1992.

Baldocchi, D. D., and K. S. Rao, Intra-field variability of scalar flux densities across a transition between desert and an irrigated potato field, *Boundary Layer Meteorol*., *76*, 109–136, 1995.

Batchelor, G. K., *The Theory of Homogeneous Turbulence*, 197 pp., Cambridge Univ. Press, New York, 1953.

Bradley, E. F., A micrometeorological study of the velocity profiles and surface drag in the region modified by a change in surface roughness, *Q. J. R. Meteorol. Soc*., *94*, 361–379, 1968.

Brutsaert, W., and M. B. Parlange, The unstable surface layer above forest: Regional evaporation and heat flux, *Water Resour. Res*., *28*, 3129–3134, 1992.

Brutsaert, W., and H. Stricker, An advection-aridity approach to estimating actual regional evaporation, *Water Resour. Res*., *15*, 443–450, 1979.

Canuto, C., M. Y. Hussaini, A. Quarteroni, and T. A. Zang, *Spectral Methods in Fluid Dynamics*, *Springer Ser. Comput. Phys*., 597 pp., Springer-Verlag, New York, 1988.

Claussen, M., The flow in a turbulent boundary layer upstream of a change in surface roughness, *Boundary Layer Meteorol*., *40*, 31–86, 1987.

Claussen, M., Estimation of areally-averaged surface fluxes, *Boundary Layer Meteorol*., *54*, 387–410, 1991.

Dabberdt, W. F., and T. W. Schlatter, Research opportunities from emerging atmospheric observing and modeling capabilities, *Bull. Am. Meteorol. Soc*., *77*, 305–323, 1996.

Deardorff, J. W., Preliminary results from numerical integrations of the unstable planetary boundary layer, *J. Atmos. Sci*., *27*, 1209–1211, 1970a.

Deardorff, J. W., Convective velocity and temperature scales for the unstable planetary boundary layer and Rayleigh convection, *J. Atmos. Sci*., *27*, 1211–1213, 1970b.

Deardorff, J. W., Numerical investigation of neutral and unstable planetary boundary layers, *J. Atmos. Sci*., *29*, 91–115, 1972.

Ferzinger, J. H., Large eddy simulation, in *Simulation and Modeling of Turbulent Flows*, edited by T. B. Gatski, M. Y. Hussaini, and J. L. Lumley, pp. 109–154, Oxford Univ. Press, New York, 1996.

Ferzinger, J. H., and M. Perić, *Computational Methods for Fluid Dynamics*, 356 pp., Springer-Verlag, New York, 1996.

Galperin, B., and S. A. Orszag, *Large Eddy Simulation of Complex Engineering and Geophysical Flows*, 600 pp., Cambridge Univ. Press, New York, 1993.

Gao, S., and D. C. Leslie, Accuracy comparison of Adams-Bashforth and leapfrog in the context of large eddy simulation, *Commun. Appl. Numer. Methods*, *6*, 1–5, 1990.

Haltiner, G. J., and R. T. Williams, *Numerical Prediction and Dynamic Meteorology*, 477 pp., J. Wiley, New York, 1990.

Hechtel, L. M., C.-H. Moeng, and R. B. Stull, The effects of nonhomogeneous surface fluxes on the convective boundary layer: A case study using large-eddy simulation, *J. Atmos. Sci*., *47*, 1722–1741, 1990.

Kaimal, J. C., and J. J. Finnigan, *Atmospheric Boundary Layer Flows*, 289 pp., Oxford Univ. Press, New York, 1994.

Katul, G. G., C.-R. Chu, M. B. Parlange, J. D. Albertson, and T. A. Ortenburger, Low-wavenumber spectral characteristics of velocity

and temperature in the atmospheric surface layer, *J. Geophys. Res*., *100*, 14,243–14,255, 1995.
Klaassen, W., Average fluxes from heterogeneous vegetated regions, *Boundary Layer Meteorol*., *58*, 329–354, 1992.
Kolmogorov, A. N., The local structure of turbulence in incompressible viscous fluid for very large Reynolds numbers (in Russian), *Dokl. Akad. Nauk SSSR*, *4*, 299–303, 1941.
Krettenauer, K., and U. Schumann, Numerical simulation of turbulent convection over wavy terrain, *J. Fluid Mech*., *237*, 261–299, 1992.
Kroon, L. J. M., and H. A. R. de Bruin, Atmosphere-vegetation interaction in local advection conditions: Effect of lower boundary conditions, *Agric. For. Meteorol*., *64*, 1–28, 1993.
Leonard, A., Energy cascade in large-eddy simulations of turbulent fluid flows, *Adv. Geophys*., *18A*, 237–249, 1974.
Mason, P. J., and N. S. Callen, On the magnitude if the subgrid-scale eddy coefficient in large-eddy simulations of turbulent channel flow, *J. Fluid Mech*., *162*, 439–462, 1986.
McComb, W. D., *The Physics of Fluid Turbulence*, 572 pp., Oxford Univ. Press, New York, 1990.
Moeng, C.-H., A large eddy simulation for the study of planetary boundary layer turbulence, *J. Atmos. Sci*., *41*, 2052–2062, 1984.
Moeng, C.-H., and J. C. Wyngaard, Statistics of conservative scalars in the convective boundary layer, *J. Atmos. Sci*., *41*, 3161–3169, 1984.
Moin, P., W. C. Reynolds, and J. H. Ferzinger, Large eddy simulation of incompressible turbulent channel flow, *Rep. TF-12*, Dep. Mech. Eng., Stanford Univ., Stanford, Calif., 1978.
Orszag, S. A., Numerical simulation of incompressible flows within simple boundaries, 1, Galerkin (spectral) representations, *Stud. Appl. Math*., *L*, 293–327, 1971a.
Orszag, S. A., Numerical simulation of incompressible flows within simple boundaries: Accuracy, *J. Fluid Mech*., *49*, 75–112, 1971b.
Orszag, S. A., and Y.-H. Pao, Numerical computation of turbulent shear flows, *Adv. Geophys*., *18A*, 224–236, 1974.
Panofsky, H. A., and A. A. Townsend, Change of terrain roughness and the wind profile, *Q. J. R. Meteorol. Soc*., *90*, 147–155, 1964.
Panton, R. L., *Incompressible Flow*, 780 pp., John Wiley, New York, 1984.
Parlange, M. B., and W. Brutsaert, Regional shear stress of broken forest from radiosonde wind profiles in the unstable surface layer, *Boundary Layer Meteorol*., *64*, 355–368, 1993.
Parlange, M. B., and G. G. Katul, An advection-aridity evaporation model, *Water Resour. Res*., *28*, 127–132, 1992.
Parlange, M. B., W. E. Eichinger, and J. D. Albertson, Regional evaporation into the atmospheric boundary layer, *Rev. Geophys*., *33*, 99–124, 1995.
Parlange, M. B., J. D. Albertson, W. E. Eichinger, A. T. Cahill, and T. J. Jackson, Evaporation: Use of fast response turbulence sensors, raman lidar and passive microwave remote sensing, in *Vadose Zone Hydrology: Cutting Across Disciplines*, edited by M. B. Parlange and J. W. Hopmans, Oxford Univ. Press, New York, in press, 1999.
Raupach, M. R., Vegetation-atmosphere interaction in homogeneous and heterogeneous terrain: Some implications of mixed layer dynamics, *Vegetatio*, *91*, 105–120, 1991.
Schmidt, H., and U. Schumann, Coherent structures of the convective boundary layer derived from large-eddy simulations, *J. Fluid Mech*., *200*, 511–562, 1989.
Segal, M., and R. W. Arritt, Nonclassical mesoscale circulations caused by surface sensible heat flux gradients, *Bull. Am. Meteorol. Soc*., *73*, 1593–1604, 1992.
Shen, S. H., and M. Y. Leclerc, How large must surface inhomogeneities be before they influence the convective boundary layer structure: A case study, *Q. J. R. Meteorol. Soc*., *121*, 1209–1228, 1995.
Smagorinsky, J., General circulation experiments with the primitive equations, 1, The basic experiment, *Mon. Weather Rev*., *91*, 99–164, 1963.
Taylor, P. A., A model of airflow above changes in surface heat flux, temperature, and roughness for neutral and unstable conditions, *Boundary Layer Meteorol*., *1*, 18–39, 1970.
Tennekes, H., and J. L. Lumley, *A First Course in Turbulence*, MIT Press, Cambridge, Mass., 1972.

J. D. Albertson, Department of Environmental Sciences, University of Virginia, Charlottesville, VA 22903. (jdalbertson@virginia.edu)
M. B. Parlange, Department of Geography and Environmental Engineering, The Johns Hopkins University, Baltimore, MD 21218.

(Received June 3, 1998; revised March 5, 1999;
accepted March 12, 1999.)